Water Eletrothermal Thruster Concept and Thrust Stand for Experiments in Parabolic Flight Campaigns - 10th EUCASS - 9th CEAS

Fabiano Perini[⋆] *and Stéphane Mazouffre*[⋆†]
[⋆]*ICARE (CNRS)*
Address
fabiano.perini@cnrs-orleans.fr · stephane.mazouffre@cnrs-orleans.fr
[†]Corresponding author

Abstract

With the rapidly increasing number of satellites in orbit, the growing complexity of their missions and the risk of collisions, there is a clear need to develop low-cost, low volume, reliable and high-thrust onboard propulsion systems. Traditionally, cold gas nitrogen systems have been used as they provide a simple solution, combining high reliability with low cost. However cold gas thrusters exhibit a fairly low specific impulse and poor storage densities. One possible way to enhance their performance is to heat the propellant in order to increase the specific impulse thus extending the mission life. When this is performed electrically with resistance heaters the thruster is known as resistojet. Resistojets are the simplest type of electrothermal thrusters. A standard propellant is hydrazine because it represents the best trade-off in terms of specific impulse, storage and distribution. Other propellants such as krypton and xenon, commonly used for Hall thrusters and ion engines, can be employed for resistojets. However, they must be stored at high pressure in specific tanks, moreover the increase in price observed in the recent years makes them commercially unattractive. Therefore, find cheap and easy-to-handle propellants is crucial for space agencies and private entities worldwide. Another propellant that seems interesting for its particular properties is pure water. Water is inexpensive, non-toxic and can be stored in liquid form. It is also an abundant resource in the solar system. Its small molecular mass makes it possible to achieve a high level of specific impulse. Although it presents some disadvantages: it has to be very pure, it must be kept from freezing and additional power is required for vaporization. Low power and low mass electrothermal water-fueled propulsion thruster and a torsional thrust balance are currently being developed at the ICARE laboratory in France. The thruster consists of a spherical tank for liquid water, a tank for the pressurizing gas (N2), a printed electronic control circuit based on the raspberry Pi microcontroller, a vaporization chamber, and a convergent-divergent nozzle for expanding the vapor. The input power remains below 50 W with a scalable thrust in the mN range and a specific impulse around 100 s. The prototype will be tested in zero-G flight, in the parabolic flight campaign next March 2024. In this contribution, we shall present the architecture of the water-fueled resistojet and the associated torsional thrust balance for measuring the thrust. We will focus especially on the vaporization chamber as it is a critical component of the propulsion system. Indeed, in the absence of gravity, vaporization must be effective to avoid droplet formation during the expansion process, therefore ensuring high performance.

1. Introduction

One of the key issues with the use of liquid water as propellant is that it fluctuates in the absence of gravity. The design of the vaporization chamber should consider this issue, because if we do not properly control the position of the water, not yet vaporized inside the chamber, a portion may end up near the outlet of the vaporization chamber without vaporization. As a result, liquid water would be present within the nozzle, reducing performance and wasting propellant. In addition, the boiling process of a liquid in the absence of gravity differs from the vaporization process that takes place on Earth. This could lead to a difference in performance between those measured in the laboratory and those experienced in orbit. A possible method for testing a thruster in weightlessness is to carry out several experimental campaigns in parabolic flight. In the ICARE laboratories of the CNRS (France), a resistojet water thruster and its thrust measurement system capable of operating in parabolic flight is under development.

2. Water Electrothermal Thruster

2.1 State of The Art

Using water as a propellant for a resistojet has been considered several times in the past decades. NASA Lewis conducted a research programme from 1987 to 1993 on possible liquid-water resistojets. Unfortunately, the programme came to an end and none of the prototypes made up to then were tested in flight. Rocketdyne and Technion began a programme to evaluate the operational characteristics of a multipropellant resistojet with operating fluids (hydrogen, helium, methane, water, nitrogen, air, argon, and carbon dioxide). Data were obtained for steam operation at a variety of power levels for each of two conditions: steam supplied to the thruster from a water vaporizer and liquid fed directly to the thruster. The decoupled system, i.e. one that uses a vaporisation chamber separate from the actual resistojet, seemed to operate in the same way as the other propellants used, in fact the fluid entering the resistojet was already vapour and only required superheating. A maximum impulse I_{sp} of 184 seconds and a thrust of 230 mN were measured, while a power consumption of 466 W in the vaporisation chamber and 692 W in the main resistojet. The coupled system required the propulsion system to operate as both a vaporizer and superheater. Therefore, the device required to operate at higher temperatures than the decoupled one causing high temperature differences between the inner wall and the fluid. This proved unfavourable as the liquid water entering the resistojet evaporated too quickly, resulting in a mixture of vapour and liquid droplets. The coupled system demonstrated a maximum specific impulse I_{sp} at a thrust level of 84 mN while consuming 289 W. The heater temperature near the nozzle under these condition was approximately 870 K.[12] One of the main problems of an electrothermal vaporizing thruster is to ensure perfect contact between liquid and solid in the absence of gravity, in fact, not taking this issue into account would result in incomplete vaporization leading to a drop in performance, in the past, several solutions have been devised to solve this problem:[15]

- **SWIRL FLOW BOILER**: In order to dry the vapor, the two-phase mixture is often swirled within the boiler, thus centrifuging the liquid to the heated wall, where it can be vaporized.

- **CROSSFLOW HEAT EXCHANGER**: The two-phase flow passes through a bank of heated tubes on which the liquid impinges and is vaporised.

- **ROTATING BOILER**: A system using a rotating vaporization chamber has many advantages. It is insensitive to gravity field and orientation. Because of the centrifugal action in the vapor space, the exit vapor has low moisture content (high quality), the liquid-vapor interface is rather sharp and stable, yielding a steady flow of both vapor and liquid. However, this system has moving parts, which increase the complexity of construction and implementation.

- **POROUS MEDIUM BOILER**: The use of porous material or a packed-bed heat exchanger to effectively vaporize the liquid. It is the same as the cross-flow heat exchanger.[14]

In recent time at the university of Tokyo, a water vaporising thruster with a vaporisation chamber and multiple nozzles has been designed, with a relatively low pressure inside the tank of 100 kPa, the throat diameter for the nozzles intended for attitude control is 1.2 mm while the nozzle intended for orbit change manoeuvres is 2.6 mm. The thruster proved to operate stably with a thrust of 1.6 mN and a specific impulse I_{sp} of approximately 70 s[1] [18] [2]. The startup ThrustMe in France has designed an electrothermal water vapor thruster with a vaporisation chamber. Tests have shown that the device is capable of achieving a specific impulse of more than 100 s and a thrust of 2 mN at a chamber temperature of 50°C and a nozzle throat diameter of 0.4 mm.[4] The Japanese company Pale Blue manufactures different kinds of water-based thrusters, in particular two types of resistojets with a power input of around 9-10 watts and a thrust of 1mN.[2] The Aurora company in Finland has developed a water-fueled mini-resistojet for collision avoidance.

2.2 Working Principles

In the literature the are mainly two types of electrothermal resistojet water thrusters, those in which the water is first vaporized in a vaporization chamber and then sent to a nozzle through a system of pipes, and those in which the nozzle head acts as both a vaporizer and a superheater. The first one is much more versatile than the second, as it allows the use of several nozzles, for the attitude control,without making the system overly complicated. Furthermore, this setting can be adopted in the realisation of hybrid propulsion devices, in which the vaporisation chamber provides water vapor not only for the nozzle of a resistojet but also for other types of systems such as gridded ion (GIT) thrusters, hall effect thrusters (HET), microwave electrothermal thrusters (MET) or helicon thrusters (HT). During this early stage of prototyping, it was decided to build a modular system with nozzle head, vaporization chamber and
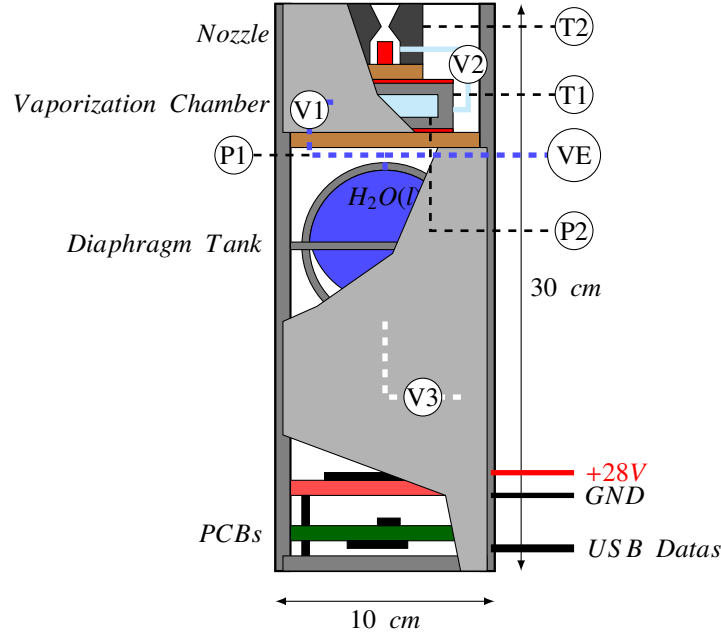
Figure 1: ICARE (CNRS) Resistojet Schematic

tank completely separated, in order to test various types of vaporization chamber and nozzle configurations. Figure 1 shows the diagram of the resistojet prototype. At the base there are two printed electronic boards, one for the thruster control and one for processing data coming from the various sensors, such as thermocouples and pressure transducers. Above the electronics is a spherical tank using a rubber diaphragm, which consists of two hemispherical caps to facilitate the installation of the bladder. The tank is thermally separated from the vaporisation chamber, that is in turn thermically isolated from the nozzle. In fact the tank, the chamber and the nozzle operate at different temperatures and if there were no thermal insulation between these three, it could induce to an elevated power loss through conduction. The vaporisation chamber is fitted with a transparent window, so that it will be possible to see if the liquid water is completely vaporised. In addition, this will also help to understand how to optimise the shape and size of the chamber. The water vapour is superheated before the converging section of the nozzle, increasing the speficic impulse of the thruster, which is proportional to the square root of the temperature, see Eqn 1.[10]

$$I_{sp} = \frac{1}{g_0} \sqrt{\frac{2\gamma}{\gamma-1} R T_{superheat} \left[1 - \left(\frac{p_e}{p_{tot}} \right)^{\frac{\gamma-1}{\gamma}} \right] \left\{ 1 + \left(1 - \frac{p_a}{p_e} \right) \frac{\gamma-1}{2\gamma} \left[\left(\frac{p_{tot}}{p_e} \right)^{\frac{\gamma-1}{\gamma}} - 1 \right]^{-1} \right\}} \tag{1}$$

Where p_{tot} is the total pressure before the converging section, p_e is the static pressure of the nozzle outlet flow, $T_{superheat}$ is the steam temperature before the converging section, R is the specific steam constant and γ is the adiabatic expansion coefficient.

Figure 2 shows that the specific impulse increases as the temperature and the nozzle surface ratio rise. Consequently, it is necessary to increase the temperature of the vapor as much as possible, but below the limit temperature that the material can withstand. In terms of the surface ratio, a compromise value must be chosen. Increasing it too much will increase the size of the thruster and may cause pressure and outlet temperature to be so low that condensation could occur. The power needed to operate the thruster is the sum of the different terms: the vaporization power, the superheating power and the power lost in conductive and radiative manner, see Eqn 2,3,4,5,6.

$$\dot{P}_{tot} = \dot{P}_{vap} + \dot{P}_{superheat} + \dot{P}_{cond} + \dot{P}_{rad} \tag{2}$$

$$\dot{P}_{superheat} = \dot{m} c_p (T_{superheat} - T_{vc}) \tag{3}$$

$$\dot{P}_{vap} = \dot{m} h_{fg} \tag{4}$$

3

WATER ELETROTHERMAL THRUSTER CONCEPT AND THRUST STAND
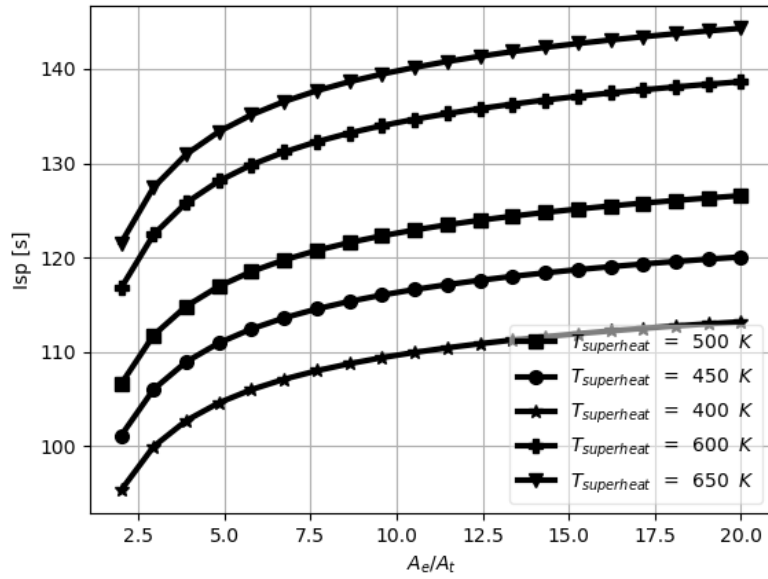
Figure 2: Specific impulse as a function of the nozzle area ratio A_e/A_t for different values of the superheating temperature $T_{superheat}$.

$$\dot{P}_{cond} \propto T_w \tag{5}$$

$$\dot{P}_{rad} \propto T_w^4 \tag{6}$$

Where $\dot{m}$ represents the mass flow rate given by Eqn 7, in the case of chocked nozzle, T_{vc} is the steam temperature in the vaporisation chamber, h_{fg} is the latent heat of vaporisation, T_w is the temperature of the heated walls.

$$\dot{m} = \frac{p_{tot}A_t}{\sqrt{\gamma R T_{superheat}}}\gamma\left(\frac{2}{\gamma+1}\right)^{\frac{\gamma+1}{2(\gamma-1)}} \tag{7}$$

Figure 4 and 3 represent the power required for vaporisation and superheating respectively for a steam temperature in the boiling chamber of $60°C$ and a throat diameter of 0.5 mm, as a function of the thrust. As can be seen, the power required for vaporisation is much higher than that for superheating, with the same thrust. As a consequence, it is essential to optimise the boiling process in the chamber in order to increase the efficiency of the thruster.

Water resistojet's operating process with vaporization chamber can be summarised by the following key points:

1. The opening of the solenoid valve located between the tank and the vaporization chamber ($V1$) for the time required to fill the latter. It necessary to calculate experimentally the amount of liquid water to be placed inside the vaporisation chamber, because a significant amount of water inside the chamber may not vaporize and end up in the nozzle with consequent loss of performance.

2. The closing of both valves, until the pressure in the vaporisation chamber is equal to the desired saturation pressure.

3. The opening of the second electrovalve ($V2$) cause the expansion of the vapour through a conventional supersonic nozzle, that continue until the pressure in the saturation chamber drops dramatically below a threshold value
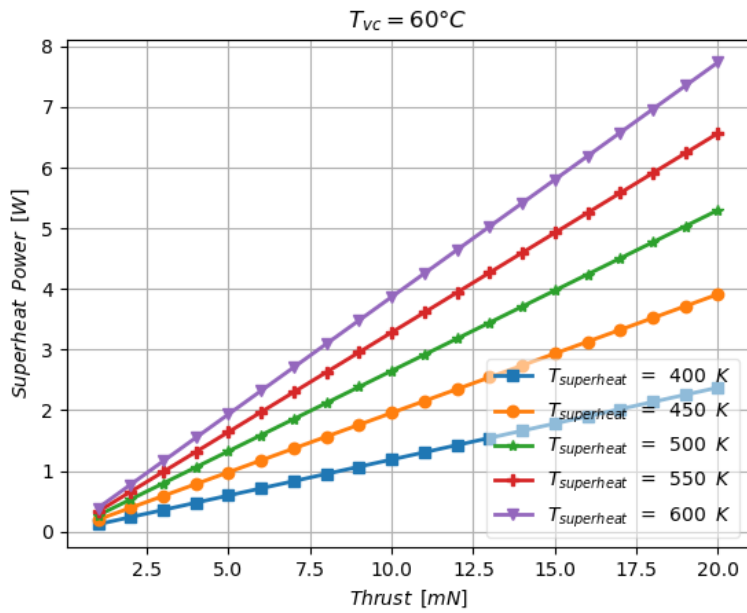
Figure 3: Superheat power vs thrust for different values of $T_{superheat}$.
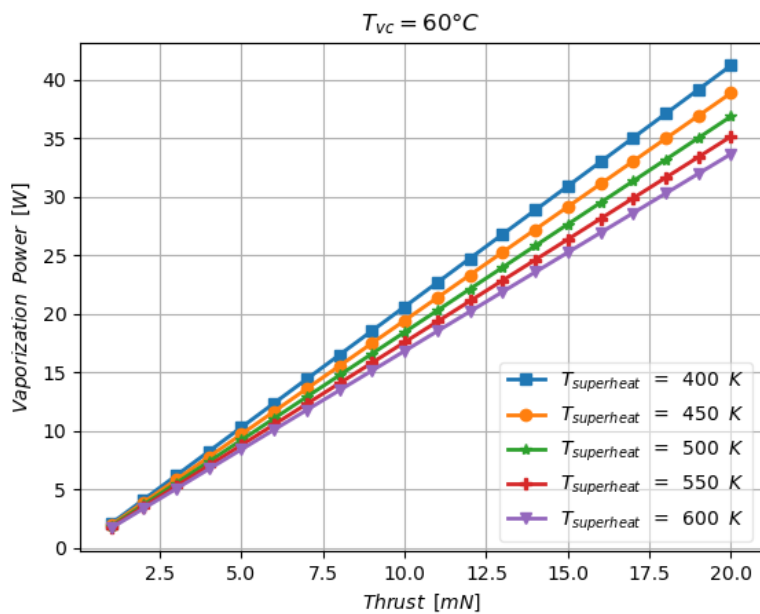
Figure 4: Vaporization power vs thrust for different values of $T_{superheat}$.
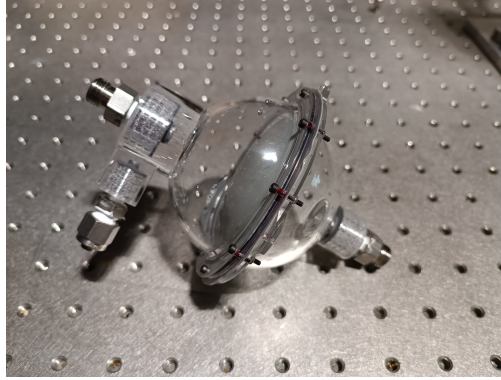
Figure 5: Transparent spherical tank with diaphragm (part in grey).

defined in the control system software. Which means that the vaporisation chamber must be filled once more with liquid water.

Throughout the process, the vapour chamber and nozzle wall temperature shall be controlled by a PID controller provided by the control system.

2.3 Liquid Water Tank

The tank has the function of storing liquid water used as propellant. Because of the lack of gravity, the floating water may not flow effectively into the vaporization chamber. There are two possibles ways to ensure that the propellant remains always near the outlet section of the tank:

- The use of a rubber bladder/diaphragm in contact with liquid on one side and with a pressurized gas such as nitrogen on the other; in this way the water will always be in contact with the bladder and with the outlet section of the tank.

- The use a porous material capable of conveying liquid water towards the outlet section of the tank.

For this prototype the first method was chosen, the diaphragm is made of commercial rubber, in order to cushion the costs. The tank has been manufactured in transparent (PMMA) material, to see if the membrane can properly discharge liquid water from the reservoir, see Figure 5.

2.4 Small-Scale Nozzle Characteristics

Even if the one-dimensional isentropic theory is a good starting point for a preliminary design of a supersonic nozzle, it loses some of its validity when the dimensions start to be in the order of mm. In fact, the fluid dynamics of small-scale nozzles differs from that of conventional large-scale thrusters in four important aspects:[11],[7]

1. The surface-to-volume ratio is orders of magnitude larger, because it scales with the inverse square root of the thrust.

2. Dissipative effects within the nozzle are no longer negligible, so the number of Reynolds scaling with the square root of the thrust is several orders of magnitude lower, as shown in Eqn 8. The thickness of the boundary layer in small nozzles is comparable with the size of the nozzle itself, so the dissipative effects are no longer negligible and the isentropic theory loses its validity. In order to optimise the shape of the nozzle, it will therefore be necessary to make fluid-dynamic simulations in the future.

3. The height of the surface roughness of the inner walls of the nozzle may be comparable with that of the inner boundary layer and even with those of the nozzle itself.

4. The hypothesis of a continuous medium may not hold as for dimensions in the mm and even μm range, the operating conditions of pressure and temperature may be such that the flow falls into a *slip regime* or even *molecular regime*.

All these aspects lead to a thickening of the boundary layer on the inner wall of the nozzle, so that the non-viscous core inside expands less than expected.

$$Re_t = \frac{u_t D_t}{\nu_t} = \frac{4\dot{m}}{\pi \mu_t D_t} = \frac{T \sqrt{C_f p_t}}{u_{eff} \mu_t \sqrt{T}} \sim \sqrt{T} \tag{8}$$

3. Torsional Thrust Balance

In the literature, there are a number of mechanisms used to measure the thrust of electric thrusters, the majority of which are based on pendulum design. The three most known are: the simple pendulum thrust balance, the inverted pendulum thrust balance[21] and the torsional pendulum thrust balance.[6] Another method that can be used is the employment of a load cell, which is nothing more than a strain gauge whose electrical resistance varies when a force is applied. The problem is that these devices are not suitable for measuring very small forces in the micro-Newton range, in addition they also need to be preloaded in order to function effectively. On the ground, preloading could be ensured by the weight of the thruster itself, in contrast, during a parabolic flight a device that can preload the cell, such as a spring, should be installed, that leads an increase of the design complexity. For these reasons the design a torsional balance from scratch was selected, and it will be tested in parabolic flight. The results of these experiments will help to understand how to improve the design, for a possible subsequent flight campaign.

3.1 Torsional Thrust Balance 3D CAD Model

Fig 6 shows the 3D CAD model of the torsional thrust stand, the components have been designed in detail in a manner that the position of the mass center can be checked using the CAD software. The load-carring structure of the balance, as well as the movable torsional arm, has been designed using $30x30mm$ aluminium profiles in order to reduce the costs of the structure. The thruster is supported by a PEEK material structure in such a way that the balance is electrically and thermally isolated from the thruster itself. The displacement is measured by an inductive sensor (LVDT), placed in the other end of the torsional pendulum arm, in order to maximise the balance's sensitivity. In the literature, there are mainly three types of displacement sensors: capacitive, inductive, and optical. The inductive sensors are the cheapest, but have a poorer resolution than the others. In order to become familiar with the control system, an LVDT sensor will be used in the first preliminary phase of experimentation, and then it can will be replaced by a capacitive or optical sensor if better resolution is required. The balance will be equipped with a voice coil for calibration and another one will be used for restoring the torsional arm position to the equilibrium. There are also counterbalance weights on the torsional arm, which allow the variation of the the gravity's center position along the axis. In this way, the thrust stand can also be used for other thruster, without incurring weight losses.
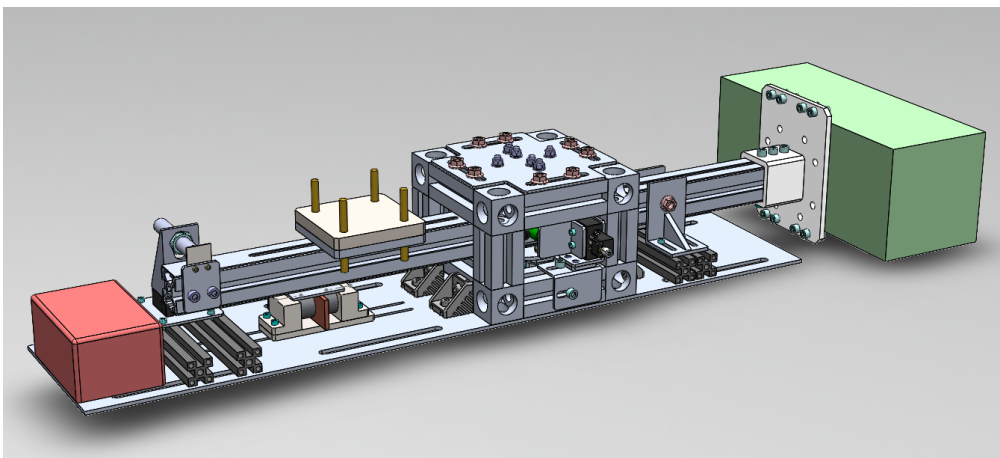
Figure 6: 3D CAD Model Torsional Thrust Stand

3.2 Torsional Thrust Balance Mathematical Model

Eqn 9 to Eqn 12 represent the set of equations used to predict the dynamic behaviour of θ angle. Eqn 9 represents the second cardinal equation of rigid-body dynamics with pole at point A[1],m_T is the total mass of the movable system, l_T l_D l_G l_{VC} are the distances of the thruster, damping system, mass centre and electric actuator from pole A, respectively; a_v is the acceleration representing the possible vibrations acting on the balance or other type of inertial forces, and I_{TOT} is the total moment of inertia.

F_D and F_{VC} are the damping force given by the passive permanent magnet system and the force of the electric linear actuator respectively, k_m is the force constant, c_{damp} is the damping coefficient, i is the current flowing in the electric motor and $l_d\dot{\theta}$ represents the velocity in the y-direction of the conductive copper plate with respect to the support holding the permanent magnets.[3]

The electromechanical equation of the voice coil is given by Eqn 12, V represents the voltage, R_{VC} and L_{VC} the resistance and inductance of the linear actuator, and k_e the counter electromotive force constant.

The torsional balance is designed to operate in a null-type and non-null-type configuration. In the null-type configuration, the voice coil actuator applies a proportional force to the thrust in order to re-establish the position of the θ angle at zero, in this way, we reduce the errors due to the thruster's misalignment. After a precise calibration the voltage or the current flowing in the coil can be linearly correlated with the thrust.

$$T(t)l_T + m_T a_v l_G - 2k\theta - F_{VC}l_{VC} - F_D l_D = I_{TOT}\ddot{\theta} \tag{9}$$

$$F_D = c_{damp}l_D\dot{\theta} \tag{10}$$

$$F_{VC} = k_m i \tag{11}$$

$$V = k_e l_{VC}\dot{\theta} + R_{VC}i + L_{VC}\frac{di}{dt} \tag{12}$$
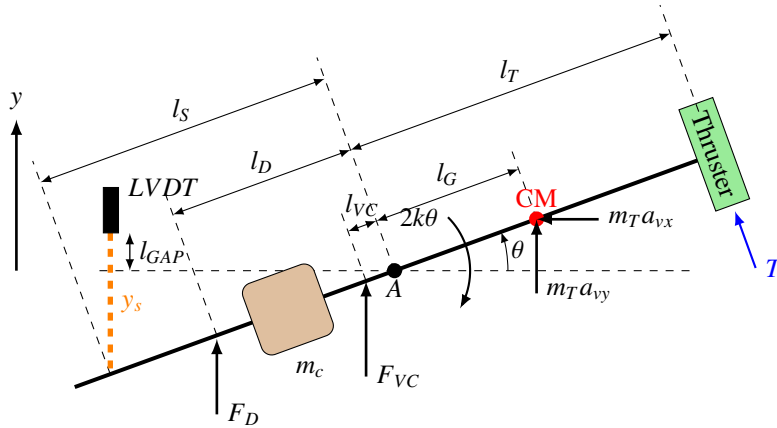
Figure 7: Balance Free Body Diagram

3.2.1 Torsional non-null-type Thrust Balance

In this configuration, we correlate the displacement measured by the sensor, which for very small angles is proportional to the thrust T. If we rewrite Eqn 9, without the vibrational torque and the torque due to the force of the electric actuator, it becomes Eqn 13. By performing the Laplace transform of both members of the equation, we obtain $\theta(s)$ as function of the thrust (T) in the laplace domain. Eqn 14.[5] [19]

$$T(t)l_T = 2k\theta + c_{damp}l_D\dot{\theta} + I_{TOT}\ddot{\theta} \tag{13}$$

---

[1]The general expression of the second cardinal equation is: $\dot{\vec{M}}_A = -m_T\vec{v}_A \wedge \vec{v}_{CM} + \vec{N}_A$ where $\vec{M}_A = m_T(CM - A) \wedge \vec{v}_A + I_A\vec{\omega}$ is the angular momentum with pole at A and $\vec{N}_A$ is the resultant momentum of the external forces.[8]

$$\theta(s) = \frac{T(s)l_T}{I_{TOT}} \frac{1}{s^2 + 2\zeta\omega_n + \omega_n^2} \tag{14}$$

where ζ and ω_n are the damping factor and the natural angular frequency of a typical second order system respectively. In a second-order system, the settling time of the step response, which is the time required for system to settle within a certain percentage of the steady state value Eqn 15, is dependent on the ω_n and ζ parameters given by Eqn 17 and Eqn 16. The angular natural frequency ω_n depends on k, the torsional spring constant and on the total moment of inertia I_{TOT} that has been calculated with the help of the CAD software. The torsional constant k is a flexure pivot parameter.

For small angles, the distance measured by the sensor is given by Eqn 18 , where l_{GAP} is the initial distance for θ equal to zero.

Figure 8 and Figure 9 show the responce to a stepped thrust applied after one second, for k equal to 0.73 and k equal to 5.45 respectively; as k increases, the settling time decreases but the value of y_s in steady state decreases, thus decreasing the sensitivity of the balance. In the zero g flight, the time duration of microgravity conditions is 22 sec. It is preferable to choose an elavated k in order to measure the thrust for a longer time duration. Regarding the damping factor, we can see that a value of 0.7 to 1.1 gives a fairly equivalent settling time.

$$\theta(t)ss = \frac{l_T T}{2k} \tag{15}$$

$$2\zeta\omega_n = \frac{c_{damp}l_D}{I_{TOT}} \tag{16}$$

$$\omega_n = \sqrt{\frac{2k}{I_{TOT}}} \tag{17}$$

$$y_s = l_{GAP} + l_s\theta \tag{18}$$
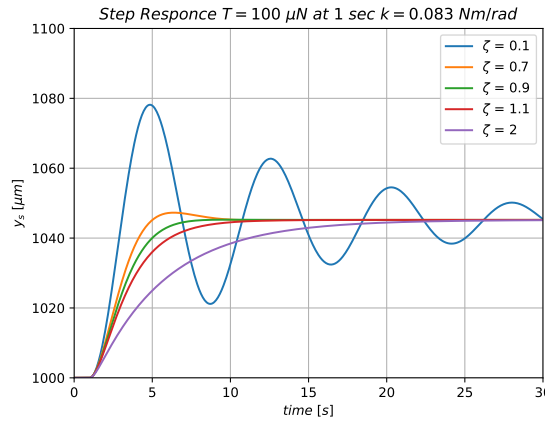
Figure 8: Step Responce for $k = 0.083 \ Nm/rad$

3.2.2 Magnetic Passive Damping

By exploiting the interaction between the magnetic and the current field in a conductor, eddy-current dampers make it possible to achieve mechanical action proportional to the velocity, compared to dampers based on the viscosity of a fluid, eddy-current dampers do not require close machining tolerances, have low temperature dependence and high linearity. They consist of a magnetic circuit and a conductor, see Figure 10. If the conductor is moving at a relative velocity $\vec{v}$ to the magnetic circuit, an electric field is generated in the areas of the conductor affected by the magnetic field, which in turn creates a current density $\vec{i}$ proportional to the electrical conductivity. The induced currents in turn interact with the magnetic field through the density Lorentz forces. The integration of Eqn 21 within the conductor

WATER ELETROTHERMAL THRUSTER CONCEPT AND THRUST STAND
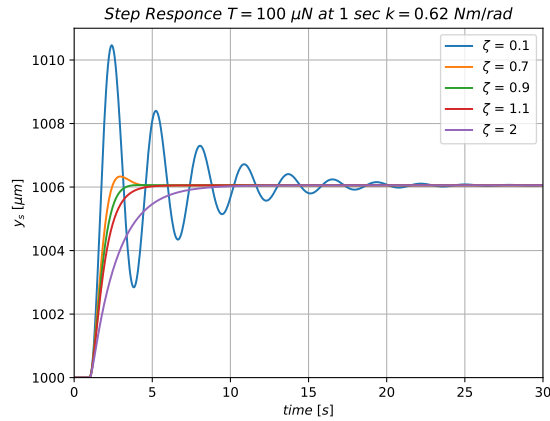
Figure 9: Step Responce for $k = 0.624\ Nm/rad$

gives the damping force. If the magnetic field is perpendicular and uniform within the conductor and the current field is two-dimensional, we have a simplified form of the damping force, given by Eqn 22. Where B_{gap} is the density of magnetic flux passing through the conductor, assumed to be uniform and perpendicular to the conductor itself, V_c is the volume of conductor crossed by the magnetic field, C_0 is a dimensionless constant that depends on the geometry of the magnets, the conductor and their relative position. Therefore, if we adopt this simplified model, the damping coefficient is given by the Eqn 25.[20] [17] [16] [9]
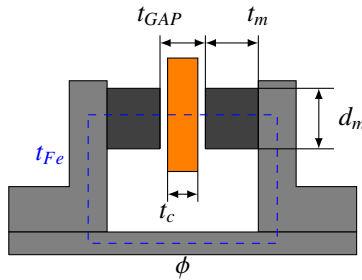
Figure 10: Magnetic Circuit Diagram

$$\vec{E} = \vec{v} \wedge \vec{B} \tag{19}$$

$$\vec{i} = \sigma \vec{E} \tag{20}$$

$$\frac{d\vec{F}}{d_{VOL}} = \vec{i} \wedge \vec{B} \tag{21}$$

$$F = C_0 \sigma B_{gap}^2 V_c \vec{v} \tag{22}$$

$$\vec{v} = l_D \dot{\theta} \hat{j} \tag{23}$$

$$M_D = F_D l_D = C_0 \sigma B_{gap}^2 V_c l_D^2 \dot{\theta} \tag{24}$$

$$c_{damp} = C_0 \sigma B_{gap}^2 V_c l_D \tag{25}$$

$$V_c = \frac{t_c d_m^2 \pi}{4} \tag{26}$$

To find a simplified expression of the magnetic field within the conductor, it is necessary to analyse a magnetic circuit in which the excitation winding has been replaced by two permanent magnets.

The Ampere's law applied to the axis line of the circuit gives, Eqn 27:[13]

$$\int_{magnets} \vec{H} \cdot \vec{dl} + \int_{gap} \vec{H} \cdot \vec{dl} + \int_{ferro} \vec{H} \cdot \vec{dl} = 2H_m t_m + H_{fe} t_{Fe} + H_{gap} t_{gap} = 0 \tag{27}$$

By substituting the B-H relations for steel (ferromagnetic), vacuum (gap) and magnets and expressing the induction magnetic field as a function of magnetic flux ϕ, which is constant, since the magnetic field is selenoidal. Assuming B uniform across the circuit cross-section, we obtain Eqn 28 and Eqn 29.

$$2\frac{B_m - B_r}{\mu_m} t_m + \frac{B_{Fe}}{\mu_{Fe}} t_{Fe} + \frac{B_{gap}}{\mu_0} t_{gap} = 0 \tag{28}$$

$$\frac{\phi}{\mu_m S_m} 2t_m - \frac{\phi_r}{\mu_m S_m} 2t_m + \frac{\phi}{\mu_{Fe} S_{Fe}} t_{Fe} + \frac{\phi}{\mu_0 S_{gap}} t_{gap} = 0 \tag{29}$$

Where $\phi_r = B_r S_m$ is the flux produced by the residual induction of the magnet (B_r), t_m, t_{gap} and t_{Fe} are the lengths of the magnets, the gap, and the ferromagnetic material on the axis line, μ is the magnetic permeability and S is the area of the various magnetic circuit sections.

Since the magnetic permeability of ferromagnetic material is much higher than that of vacuum, we can neglect the third term in Eqn 29. Assuming that $S_{gap} = S_m$ and $\mu_m = \mu_0$, Eqn 29, it is simplified into the Eqn 30.

$$\phi = \frac{\phi_r}{1 + \frac{t_{gap}}{2t_m}} = B_{gap} S_{gap} \tag{30}$$

Table 1 summarises the values of the various damping system parameters to achieve a damping factor $\zeta = 0.8$.

Table 1: Passive Eddy Current Parameters

	Value	**Unit**
σ	5.96e07	S/m
t_c	0.0035	m
d_m	20e-03	m
b	0.024	m
d	0.05	m
C_0	0.3604	
B_r	14400e-04	T
t_{gap}	0.005	m
t_m	15e-03	m

3.2.3 Torsional null-type Thrust Balance Matlab/Simulink Model

To facilitate the implementation of the model in Matlab/Simulink, Eqn 9 and Eqn 12, have been reworked to make explicit the second derivative of θ and the derivative of the current i, Eqn 31 and Eqn 32. The linear electric motor is controlled by an H-bridge driver for DC motors, a microcontroller supplies the driver with a PWM signal as input, the output will always be a PWM signal of V_{dd} that is the supply voltage. The H-bridge allows the required current to be supplied to the voice coil, which is usually much higher than the current that a microcontroller can withstand.

Fig 11 and Fig 12 represent the Simulink diagrams of Eqn 31 Eqn 32 respectively, for integration we used a discrete integral block with forward Euler method and sampling time equal to T_s.

Fig 14 shows the microcontroller's Simmulink block, the continuous voltage signal from the LVDT sensor is processed by the ADC (Analog Digital Converter). The output from the ADC is a quantized voltage that will be transformed into a quantized θ. The discrete PID controller will provide the necessary duty cycle for the PWM signal so that the reference theta is zero. The PWM signal is multiplied by the value of the supply voltage to simulate the H-bridge. The output signal from the PID controller block can be negative or positive depending on whether the force required to re-establish the position of the torsional arm is negative or positive. Therefore, we have taken this into account by placing a Matlab function block which allows us to invert the polarity of the supply voltage. To decide the resolution and sampling time T_s of the ADC two simulations were carried out, one with the analogue digital converter and one without it. Fig 15 and Fig 16 show the displacement and the average current required by the actuator, with

WATER ELETROTHERMAL THRUSTER CONCEPT AND THRUST STAND

a sampling time $T_s = 0.00001s$ and with a resolution of 16 bit we obtain good results. The period of the PWM signal was chosen to be quite lower than the sampling period. The PID parameters were tuned through Simulink's autotuning method, the discrete transfer function $PID(z)$, in the z-transform, will then be converted into a finite difference equation that is easy to implement in a microcontroller code. Table 2 shows all the parameters' values of the mathematical model of the torsional thrust balance.
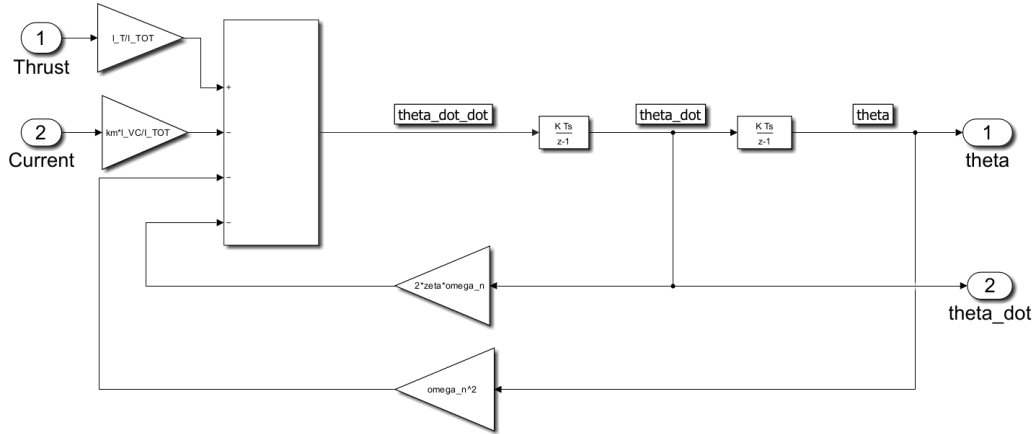
Figure 11: Simulink Mechanical Diagram
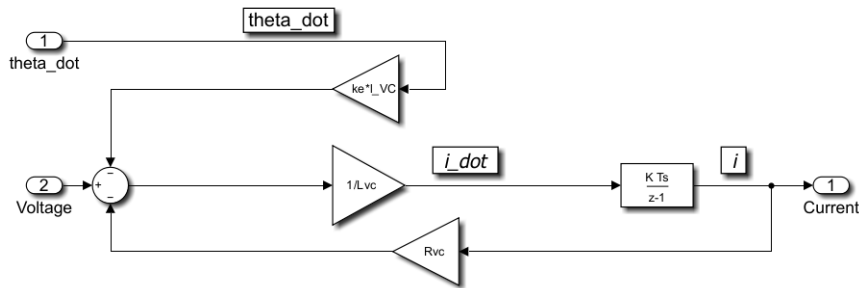
Figure 12: Simulink Voice Coil Diagram
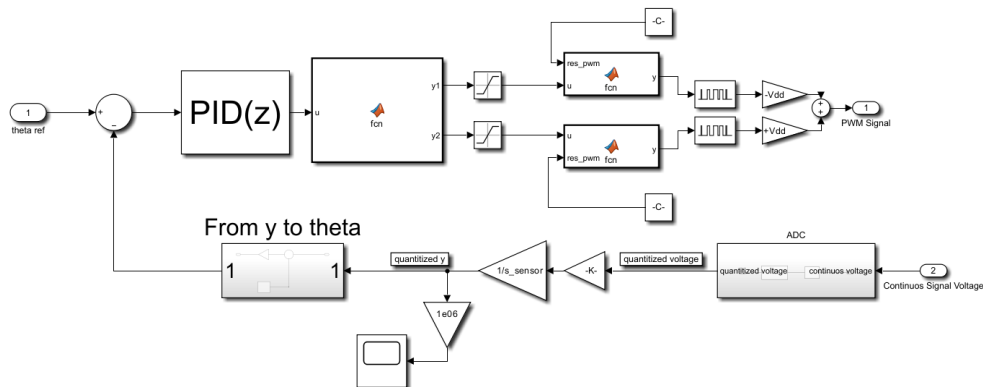
Figure 13: Simulink Microcontroller Diagram

$$\ddot{\theta} = -2\zeta\omega_n\dot{\theta} - \omega_n^2\theta - \frac{k_m i l_{VC}}{I_{TOT}} + \frac{T l_T}{I_{TOT}} \tag{31}$$
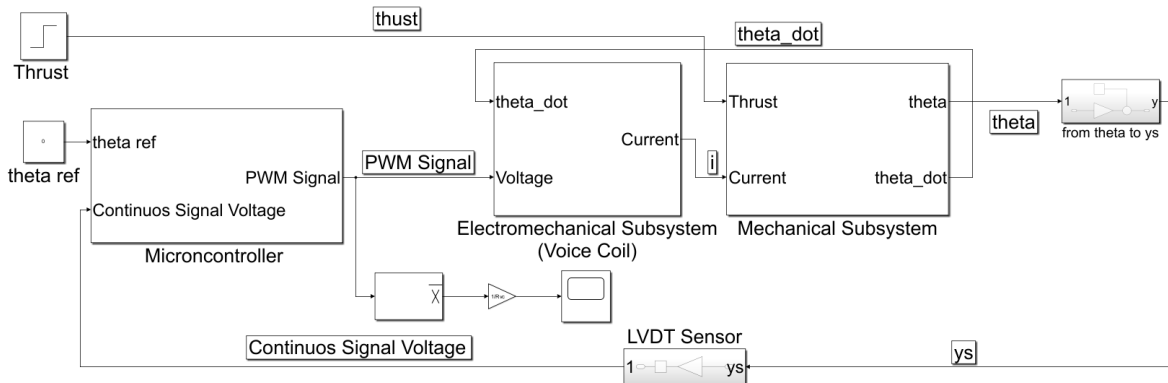
Figure 14: Simulink Model Diagram
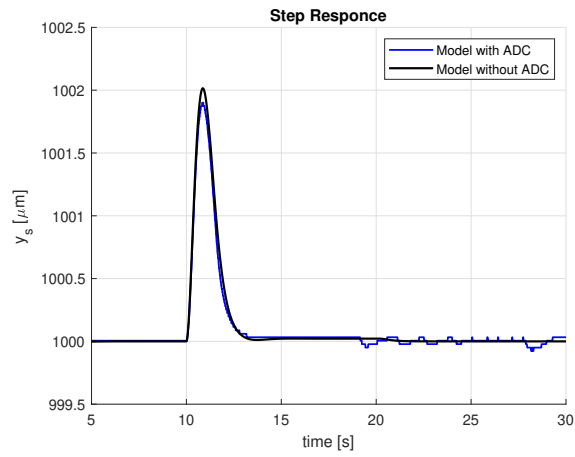
Figure 15: Step Responce PID Controller (displacement) T=0.1mN
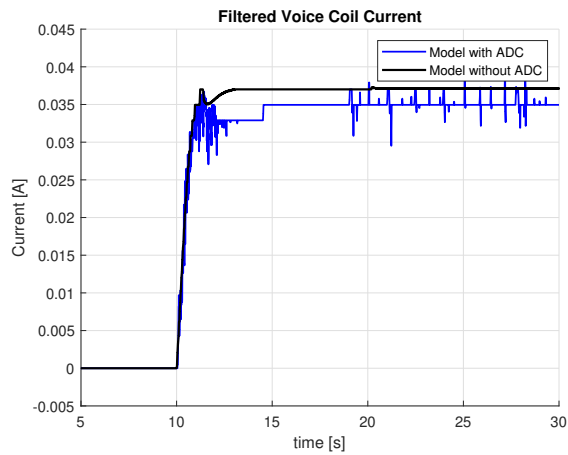
Figure 16: Step Responce PID Controller (current) T=0.1mN

$$\frac{di}{dt} = \frac{V - k_e l_{VC} \dot{\theta} - i R_{VC}}{L_{VC}} \tag{32}$$

Table 2: Torsional Thrust Balance Parameters

	Value	**Unit**
l_T	0.275	m
l_D	0.15	m
c_{damp}	6.72	kg/s
k_m	0.74	N/A
R_{VC}	1.9	Ω
L_{VC}	167e-06	H
k_e	0.69	V/ms
ω_n	2.2959	rad/sec
ζ	0.8	
Ts	0.00001	s
f_{PWM}	1000	Hz
ADC	16	bit

4. Conclusion

Water, the green propellant par excellence, is becoming an attractive alternative to various common propellants, such as hydrazine. Private and public space entities are starting to invest in research into water-fueled thrusters. This article presents the architecture of a liquid water resistojet thruster and the thrust stand measurement system. In the coming months, the prototype will be tested at the ICARE laboratories of the CNRS in Orléans. An experimental campaign in parabolic flight is planned in March 2024. The objective of the experimental campaign in microgravity is to test different vaporisation chambers in order to optimise their shape and size. Details concerning the specific architecture of the various components will be given in forthcoming publications.

5. Acknowledgements

References

[1] Jun Asakawa, Hiroyuki Koizumi, Keita Nishii, Naoki Takeda, Masaya Murohara, Ryu Funase, and Kimiya Komurasaki. Fundamental ground experiment of a water resistojet propulsion system: Aquarius installed on a 6u cubesat: Equuleus. *Transactions of the Japan Society for Aeronautical and Space Sciences, Aerospace Technology Japan*, 16(5):427–431, 2018.

[2] Jun Asakawa, Hiroyuki Koizumi, Kazuya Yaginuma, and Yuichi Nakagawa. Pre-flight testing results of multiple water propulsion systems-resistojet and ion thruster for smallsats. 2022.

[3] Federico Baronti, A Lazzeri, F Lenzi, Roberto Roncella, Roberto Saletti, and Sergio Saponara. Voice coil actuators: From model and simulation to automotive application. In *2009 35th Annual Conference of IEEE Industrial Electronics*, pages 1805–1810. IEEE, 2009.

[4] Fernanda Pimenta Cyrne Giulio Coral Francesco Mattia Bianchi, Elena Zorzoli Rossi. *Proof of concept and preliminary design of a superheated water vapor thruster*. first edition, 2022.

[5] Gene F. Franklin, J. David Powell, and Abbas Emami-Naeini. *Feedback Control of Dynamics Systems*. Pearson Higher Education, 2010.

[6] Manuel Gamero-Castano. A torsional balance for the characterization of micronewton thrusters. *Review of scientific instruments*, 74(10):4509–4514, 2003.

[7] STANLEY GRISNIK, TAMARA SMITH, and LARRY SALTZ. Experimental study of low reynolds number nozzles. In *19th International Electric Propulsion Conference*, page 992, 1987.

[8] Giovanni Federico Gronchi. Lezioni di meccanica razionale. 2016.

[9] Mark A Heald. Magnetic braking: Improved theory. *American journal of physics*, 56(6):521–522, 1988.

[10] Philip G Hill and Carl R Peterson. Mechanics and thermodynamics of propulsion. *Reading*, 1992.

[11] Federico la Torre. *Gas Flow in Miniaturized Nozzles for Micro-Thrusters*.

[12] Timothy J Lawrence. *Research into resistojet rockets for small satellite applications*. University of Surrey (United Kingdom), 1998.

[13] Corrado Mencuccini and Vittorio Silvestrini. *Fisica: elettromagnetismo e ottica: con esempi ed esercizi*. CEA, 2017.

[14] WEARL MORREN. Preliminary characterizations of a water vaporizer for resistojet applications. In *28th Joint Propulsion Conference and Exhibit*, page 3533, 1992.

[15] WEARL MORREN and JAMES STONE. Development of a liquid-fed water resistojet. In *24th Joint Propulsion Conference*, page 3288, 1987.

[16] Kosuke Nagaya. On a magnetic damper consisting of a circular magnetic flux and a conductor of arbitrary shape. part ii: applications and numerical results. 1984.

[17] Kosuke Nagaya and Hiroyuki Kojima. On a magnetic damper consisting of a circular magnetic flux and a conductor of arbitrary shape. part i: derivation of the damping coefficients. 1984.

[18] Keita Nishii, Jun Asakawa, Kosei Kikuchi, Mariko Akiyama, Qihang Wang, Masaya Murohara, Yasuho Ataka, Hiroyuki Koizumi, Ryu Funase, and Kimiya Komurasaki. Flight model development and ground demonstration of water resistojet propulsion system for cubesats. *Transactions of the Japan Society for Aeronautical and Space Sciences*, 63(4):141–150, 2020.

[19] Katsuhiko Ogata and Yanjuan Yang. Modern control engineering. 1970.

[20] Andrea Tonoli, Andrea Festini, E Zenerino, et al. Controllo delle vibrazioni di strutture flessibili mediante smorzatori dinamici a correnti parassite. *XXX Convegno Nazionale AIAS, Alghero (SS)*, pages 12–15, 2001.

[21] TF Yang, Ping Liu, FR Chang-Díaz, Harvey Lander, RA Childs, HD Becker, and SA Fairfax. A double pendulum plasma thrust balance and thrust measurement at a tandem mirror exhaust. *Review of scientific instruments*, 66(9):4637–4643, 1995.